RSC Advances

PAPER

View Article Online
View Journal | View Issue



Cite this: *RSC Adv.*, 2025, **15**, 46541

# Novel core–shell $Fe_3O_4$/NiO nanofibers for the photocatalytic degradation of active pharmaceutical compounds

Roman Viter, *[a] Mahmoud Abid,[b] Tia Maria Howayek,[b] Viktor Zabolotnii,[a] Martin Sahul,[c] Mária Čaplovičová,[d] Iryna Tepliakova,[a] Viesturs Sints,[a] Aleksandrs Dutovs,[a] Donats Erts,[a] Ambra Fioravanti,[e] Simonas Ramanavicius,[af] Roland Habchi,[g] David Cornu[b] and Mikhael Bechelany *[bh]

Coaxial electrospinning is a facile and versatile method for the fabrication of core–shell metal oxides for environmental applications. The use of core–shell metal oxide nanofibers with a magnetic core and photocatalytic shell is a new approach for the photocatalytic degradation of active pharmaceutical compounds (APCs) in water and the removal of photocatalysts by a magnetic field. In the present work, we report the fabrication and characterization of novel $Fe_3O_4$–$Fe_2NiO_4$/NiO core–shell nanofibers with advanced structural, optical, magnetic and photocatalytic properties *via* co-axial electrospinning. The aim of this work is to investigate the photocatalytic degradation of acetaminophen by the novel metal oxide core–shell nanofibers with different structural properties. The core–shell nanofibers were fabricated using constant core solution parameters (PAN 7.55% w/w and Fe nitrate 5.5% w/w) and variable shell solution parameters (PVP 11.4–11.1% w/w and Ni acetate 5.29–8.51% w/w). The phase transition of $Fe_3O_4$ → $Fe_2NiO_4$ was observed in the core. The $Fe_3O_4$–$Fe_2NiO_4$/NiO nanofibers exhibit a high optical absorption in the visible range (band gaps of 2 eV and 2.2 eV), significant magnetization (15 A $m^2$ $kg^{-1}$) and high efficiency for the degradation of methylene blue (80%) and acetaminophen (45%). The photocatalytic properties of the $Fe_3O_4$–$Fe_2NiO_4$/NiO nanofibers significantly depended on their core and shell chemical composition. The formation of spinel $Fe_2NiO_4$ in the core was one of the factors that limited the photocatalytic performance of the core–shell nanofibers. Thus, their photocatalytic performance could be improved by adjusting the core and shell fabrication parameters. The advanced properties of the $Fe_3O_4$–$Fe_2NiO_4$/NiO core–shell nanofibers highlight their applications for the efficient degradation of active pharmaceutical compounds in water resources.

Received 7th July 2025
Accepted 9th November 2025

DOI: 10.1039/d5ra04859a

rsc.li/rsc-advances



## 1 Introduction

The contamination of water resources by active pharmaceutical compounds (APCs) has become a pressing environmental issue. APCs significantly change the water environment and increase antibiotic resistance in humans.[1,2] Therefore, the efficient degradation of APCs in water resources has become a recent global focus.[3,4]

Recently, we have reported the use of electrospun nanofibers for the photocatalytic degradation of APCs in water.[3–5] Indeed, the photocatalytic properties of metal oxide (MOX) nanofibers have been controlled by doping and varying the technological parameters of the deposition.[6] The developed MOX nanofibers showed high rates of APC degradation under visible light conditions.[1,7] One of the restrictions of the developed MOX nanofibers in real applications is the difficulty in removing them from water sources.[8] Thus, new MOX nanofibers with advanced optical, magnetic and photocatalytic properties could be a promising solution for the degradation and removal of APCs from water sources by using a magnetic field.

Coaxial electrospinning is a powerful method for the fabrication of core–shell nanostructures with tailored properties.[9–12] Coaxial electrospinning enables the production of functional nanomaterials, like metal oxides, metal/metal nanofibers and

[a]*Faculty of Science and Technology, University of Latvia, 19 Raina Blvd, Riga LV 1586, Latvia*

[b]*Institut Européen des Membranes, IEM, UMR, Univ Montpellier, ENSCM, CNRS, 5635, Montpellier, France. E-mail: mikhael.bechelany@umontpellier.fr*

[c]*Institute of Materials Science, Slovak University of Technology in Bratislava, Jána Bottu 25, 917 24 Trnava, Slovakia*

[d]*Centre for Nanodiagnostics of Materials, Slovak University of Technology in Bratislava, Vazovova 5, 812 43 Bratislava, Slovakia*

[e]*Institute of Sciences and Technologies for Sustainable Energy and Mobility (STEMS), National Research Council (CNR), Via Canal Bianco, 28, 44124, Ferrara, Italy*

[f]*Department of Electrochemical Material Science, Centre for Physical Sciences and Technology, Sauletekio Av. 3, LT-10257 Vilnius, Lithuania*

[g]*Faculty of Sciences 2, EC2M, Lebanese University Campus Pierre Gemayel, Fanar, 90656, Lebanon*

[h]*Functional Materials Group, Gulf University for Science and Technology, Mubarak Al-Abdullah, Kuwait*

hollow metal oxide nanotubes.[9–12] Novel core–shell MOX nanofibers show new optical properties due to the presence of defects on their interface and enhanced charge separation and surface properties.[6,13] Most recently, $ZnO/In_2O_3$, $SnO_2/In_2O_3$, and $TiO_2$ core–shell nanofibers have been tested as gas sensors and in catalysis applications.[6,13]

The fabrication of magnetic-optical core–shell nanofibers by coaxial electrospinning for photocatalytic applications is quite challenging. Iron oxides are typical materials used as the magnetic core in other methods.[14,15] It is known that iron tends to form non-magnetic spinels with other oxides under high-temperature treatment (over 500 °C).[16] However, its interdiffusion and spinel layer effects on the optical, magnetic and photocatalytic properties of core–shell nanofibers have not been studied to date. Recent reports showed the successful fabrication of Ni/C, $Fe_3O_4$/C and Ni–Co spinel nanofibers *via* the coaxial electrospinning method.[17–21] However, no reports on the fabrication, design, and main properties of magnetic metal oxide/metal oxide nanofibers have been published to date.

Recently, we reported the fabrication of core–shell $ZnFe_2O_4$/ZnO nanofibers *via* coaxial electrospinning.[16] It was found that the obtained samples showed no magnetic properties. Due to the formation of spinel, the core of the fiber was composed of $ZnFe_2O_4$ with a diameter of 120 nm, and the ZnO shell was composed of ZnO particles with an average size of 20–30 nm. The samples showed good photoelectrochemical properties. However, the primary goal of achieving magnetic metal oxide/metal oxide nanofibers with advanced optical and magnetic properties was not realized.

Transition metals and their oxides (NiO, $MoO_2$, $MnO_2$, and $Co_3O_4$) are promising materials for energy, multi-functional materials,[22–24] sensor, photoelectrocatalytic and photocatalytic[17,18,25–30] applications. Due to their different oxidation states, they show enhanced interaction with target molecules and high photocatalytic performance.

$Fe_3O_4$/NiO core–shell nanoparticles with advanced optical, magnetic and photocatalytic properties have been widely investigated.[31–33] They demonstrated good photocatalytic performances and their significant removal from water achieved using a magnetic field. The fabrication of $Fe_3O_4$/NiO core–shell nanoparticles requires multistep procedures with high dependence on the fabrication parameters, such as concentration of core and shell precursors, pH of solution and annealing temperature.[8,34,35] Conversely, the coaxial fabrication of core–shell metal oxide nanofibers only requires two steps. It depends on the concentration of the core and shell solutions, pumping speed and annealing temperature. Our previous experience showed that the fabrication of $Fe_3O_4$/NiO core–shell nanofibers with advanced properties is a new topic to investigate. Also, opto-magnetic $Fe_3O_4$/NiO core–shell nanofibers have never been tested as visible light photocatalysts for the degradation of APCs.

Herein, we report the development of novel core–shell metal oxide nanofibers with advanced properties *via* co-axial electrospinning. The effects of the core and shell solutions on forming the structure and optical and magnetic properties of the metal oxide core–shell nanofibers have been studied. Also, the photocatalytic degradation of methylene blue and acetaminophen by the novel core–shell nanofibers under visible light excitation has been investigated. Subsequently, the effect of phase transitions ($Fe_3O_4$/NiO to $Fe_2NiO_4$) in the core–shell nanofibers on their optical, magnetic and photocatalytic properties have been discussed.

# 2 Experimental

## 2.1 Materials

Polyvinylpyrrolidone (PVP) ($M_w$: 1 300 000) (CAS No: 9003-39-8), polyacrylonitrile (PAN) (CAS No: 25014-41-9), *N*,*N*-dimethylformamide (DMF) (CAS No: 68-12-2), $Fe(NO_3)_2 \cdot 9H_2O$ (CAS No: 7782-61-8), nickel acetate (NiAc) (CAS No: 6018-89-9), and acetaminophen (ACT, CAS No: 103-90-2) were purchased from Sigma Aldrich.

Methylene blue hydrate (MB < CAS: 122965-43-9), 2-propanol (99.9%, CAS: 67-63-0), *p*-benzoquinone ($C_6H_4O_2$, ≥99.5%, CAS:106-51-4) and ethylenediaminetetraacetic acid (EDTA, 99.995%, CAS: 60-00-4) were from Sigma-Aldrich.

## 2.2 Solution fabrication

The core solution (Solution A) was prepared as follows: DMF (4 mL) was heated to 75 °C. Then, PAN (0.41 g) was added to the hot DMF and stirred (Solution 1). DMF (1 mL) and $Fe(NO_3)_2$ (0.3 g) were mixed and ultrasonicated for 15 min (Solution 2). When PAN in Solution 1 was fully dissolved, Solution 2 was added to Solution 1 under continuous stirring. The fabricated Solution A was stirred overnight at room temperature.

The shell solution (Solution B) was prepared as follows: DMF (3 mL) was heated to 50 °C. Then, PVP (0.65 g) was added to the hot DMF and stirred (Solution 3). DMF (2 mL) and metal salts (NiAc (0.3–0.5 g)) were mixed and ultrasonicated for 30 min (Solution 4). When the PVP in Solution 3 was fully dissolved, Solution 4 was added to Solution 3 under continuous stirring. The fabricated Solution B was stirred overnight at room temperature.

The parameters of Solution A and B were recalculated using the weight fraction ($w/w_{solution}$) of polymers and metal precursors. The deposited samples had the following parameters:

FeNi33: PAN 7.55% and Fe 5.5% (0.3 g Fe nitrate)/PVP 11.4% and Ni 5.29% (0.3 g Ni acetate);

FeNi34: PAN 7.55% and Fe 5.5% (0.3 g Fe nitrate)/PVP 11.26% and Ni 6.93% (0.4 g Ni acetate);

FeNi35: PAN 7.55% and Fe 5.5% (0.3 g Fe nitrate)/PVP 11.1% and Ni 8.51% (0.5 g Ni acetate).

## 2.3 Electrospinning

Solutions A and B were loaded in separate 5 mL plastic syringes and attached to a coaxial needle (Linari Engineering, Pisa, Italy) with plastic tubes. The coaxial needle had an inner diameter of 0.5 mm and an outer diameter of 1 mm. The syringes were installed in two independent syringe pumps and set up with pump rates of 450 μL per h (Solution A) and 600 μL per h (Solution B). The needle was installed in the spinning camera 20 cm above the collector. The collector was covered by an

 

aluminum foil. The rotating speed of the collector was 200 rpm. The voltage applied between the needle and the collector was 20 kV.

Control samples of NiO nanotubes and iron oxide nanofibers were deposited without metal precursors in the core and shell, respectively. The control samples of iron core/empty shell and empty core/nickel shell are denoted as FeNF and NiNT, respectively.

The as-prepared nanofibers were dried under vacuum overnight at room temperature and annealed at 500 °C for 1 h. The control NiO nanotube and iron oxide nanofiber samples were deposited as mentioned above without precursors in the core and shell, respectively.

### 2.4 Characterization

X-ray diffraction (Bruker D8 diffractometer, CuKa radiation, Germany) was applied to identify the phases of the developed core–shell nanofibers. To analyze the molecular vibrations and bonds in the obtained materials, Raman spectroscopy measurements were performed on a WiTeC Alpha 300R microRaman system equipped with a laser (532 nm excitation wavelength). X-ray photoelectron spectroscopy (XPS) was used for oxidation state evaluation and chemical shift determination using a Thermo Fisher Scientific Escalab $Xi^+$ spectrometer under high vacuum conditions. The samples were deposited on carbon pads, and any loose material was removed with high-velocity airflow. Charge compensation (flood gun, standard mode) and surface etching (ion gun, mild conditions for 10 s) were used to remove surface contamination and reduce surface charging. XPS data were analyzed using the Avantage 5.2995 software, and the adventitious carbon peak at 284.8 eV was used as the calibration point.

The structural properties of the deposited nanofibers were investigated by SEM (Hitachi, Japan) and TEM/EDX (JEOL, Japan).

The optical properties of the core–shell nanofibers were studied by diffuse reflectance spectroscopy in the UV-visible range using an Ocean Optics fiber optic light source (DH2000, 250–900 nm, USA), integrating sphere (Ocean Optics, IS-8, USA) and fiber optic spectrometer (Ocean Optics HR4000, USA).

The magnetic properties of the samples were characterized by vibrating sample magnetometry (VSM). Measurements were performed using a Lake Shore Cryotronics Co., model 7404 VSM vibrational sample magnetometer. A magnetizing field in the range of −1 T to 1 T was applied in a sequence starting with zero field, and then sweeping through the range twice, enabling both zero field susceptibility and any possible hysteresis to be recorded. The sample holders were found to have non-negligible magnetic properties (especially in the case of less magnetic samples), and therefore the magnetization of each holder was measured prior to sample measurements and subtracted from the results.

Electrochemical measurements were carried out using an Autolab PGSTAT302 potentiostat operated in potentiostatic mode (potential scan). A 3-electrode cell configuration was used, consisting of the following electrodes: WE – sample, RE – Ag/AgCl (3 M KCl), and CE – Pt wire. The measurements were conducted within the potential range of −0.3 to 1.5 V *vs.* Ag/AgCl, over the frequency range of 20 000 to 5000 Hz. A 1 M KOH aqueous solution was used as the electrolyte.

### 2.5 Photocatalysis tests and kinetic measurements

Photocatalytic degradation experiments were carried out using a custom-built photoreactor equipped with a visible-light halogen lamp (R7S Quartz Linear, 400 W, 3000 K, 220–240 V, 118 mm, Ref: 2430800281468), emitting predominantly within the 400–700 nm range, with negligible UV contribution. The lamp-to-solution distance was consistently set at 10 cm, and the reaction temperature was maintained at 20–25 °C *via* a circulating cold-water system. In a typical procedure, 50 mg of core–shell nanofibers was dispersed in 100 mL of an aqueous solution containing 10 ppm of the target pollutant (MB or ACT), stirred in the dark for 30 min to establish adsorption–desorption equilibrium, and subsequently irradiated under visible light. Aliquots (2 mL) were collected at 30 min for visible light, and then filtered through 0.45 μm membranes, depending on the target molecule. The ACT degradation intermediates and products were further analyzed using a high-performance liquid chromatography (HPLC) system equipped with a C18 reverse-phase column (Nucleoshell RP18) and a Quattro-Micro mass spectrometer with an electrospray ionization source (Waters Micromass, UK). Photocatalytic efficiency was assessed using eqn (1), as described in ref. 5 and 36.

$$\text{Degradation efficiency } (\%) = \left[\frac{C_0 - C}{C_0}\right] \times 100 \quad (1)$$

where $C_0$ and $C$ are the pollutant concentrations before and after irradiation, respectively. Additionally, the kinetics of photocatalytic degradation under visible light were evaluated using a pseudo-first-order model expressed as eqn (2), as follows:[5,36]

$$\ln(C_0/C) = K_{app}t \quad (2)$$

where $C_0$ is the initial concentration, $C$ the concentration at the time $t$, and $K_{app}$ is the apparent rate constant.

## 3 Results

The SEM images of FeNi33, FeNi34 and FeNi35 are presented in Fig. 1a–c, respectively. The SEM images show well-shaped nanofibers fabricated by electrospinning. The dimensions of the fibers were 183 ± 38 nm, 200 ± 24 nm and 232 ± 41 nm for FeNi33, FeNi34 and FeNi35, respectively. The average length of the nanofibers is 8 μm.

The XRD spectra of the core–shell nanofibers are shown in Fig. 2a. Analysis of the XRD spectra showed that $Fe_2O_3$ is formed in the case of the control FeNF nanofibers (Fig. 2a) (PDF standard card JCPDS#33-0664), whereas $Fe_3O_4$ is formed in the core–shell nanofibers (Fig. 2a) (PDF standard card JCPDS#19-0629). An NiO phase was identified in the NiNT and FeNi nanostructures (Fig. 2a) (PDF standard card JCPDS#47-1049). The full width at half maximum (FWHM) of the XRD peaks of

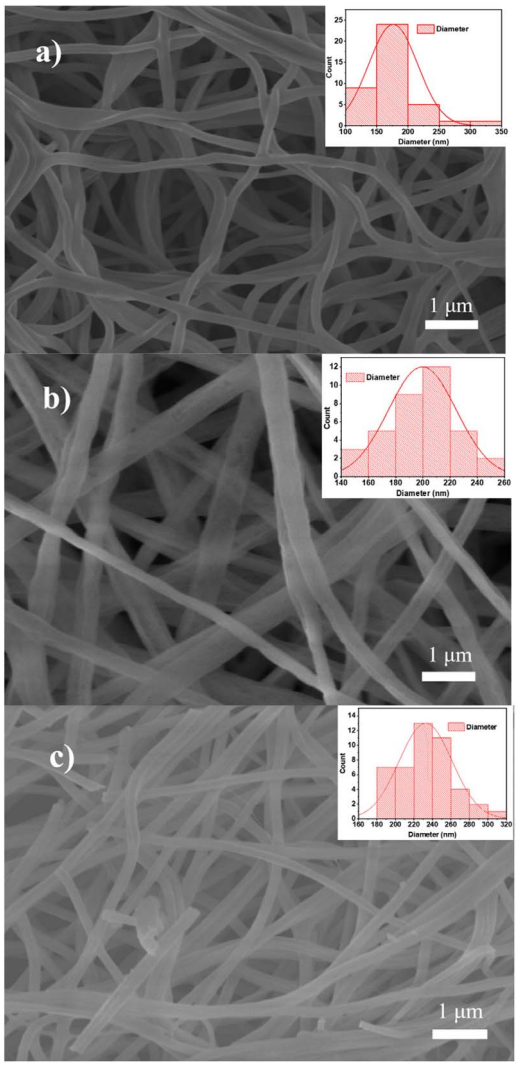


Fig. 1 Structural properties of the core–shell nanofibers, measured by SEM: (a) FeNi33, (b) FeNi34, and (c) FeNi35.

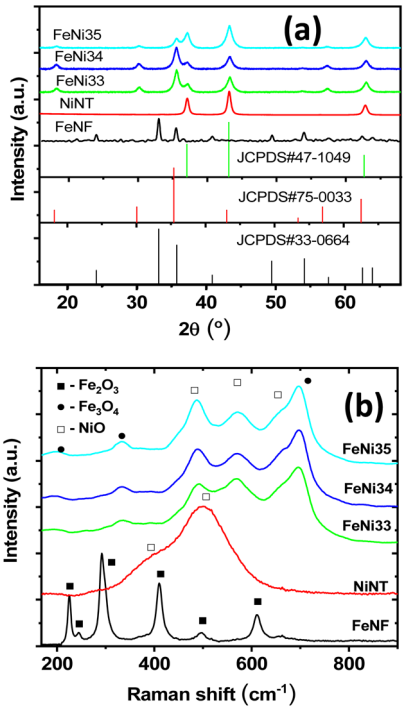


Fig. 2 Structural properties of the core–shell nanofibers measured by (a) XRD and (b) Raman.

NiO slightly increased for the core–shell FeNi nanostructures compared to NiNT. Given that no correlation between the [Fe/Ni] concentration ratio and FWHM was found, we assume that the peak widening could be explained by the lattice strain at the interface of $Fe_3O_4$/NiO. Analysis of the XRD peaks of the core–shell nanofibers showed an increase in the NiO peak intensity with an increase in the [Ni/Fe] concentration ratio, indicating an increase in the shell thickness.

Fig. 2b shows the Raman spectra of the core–shell nanofibers, NiO nanotubes and iron oxide nanofibers. The Raman peaks identified at 223, 291, 409, 496 and 611 $cm^{-1}$ (Fig. 2b) represent the $A_{g1}$, $E_{g1}$, $E_{g1}$, $A_{g1}$ and $E_{g1}$ vibrational modes of $Fe_2O_3$.[37] The Raman spectrum of the NiO nanotubes (Fig. 2b) showed peaks located at 401 $cm^{-1}$ (1P-TO), 499 $cm^{-1}$ (1P-M) and 599 $cm^{-1}$ (1P LO), confirming the presence of the NiO phase.[38]

The Raman spectra of the core–shell nanofibers (Fig. 2b, curves 3–5) showed a significant difference from the Raman peaks related to pristine $Fe_2O_3$ and NiO. The peaks located at 198 ($T_{2g}(1)$), 328 ($E_g$) and 698 $cm^{-1}$ ($A_{g1}$) correspond to the $Fe_3O_4$ phase,[39,40] showing good agreement with the XRD measurements.[41,42] The Raman peaks assigned at 465 (1P-TO), 544 (1P + 1M) and 659 $cm^{-1}$ (1P LO) correspond to NiO.[38,43,44]

In our previous work,[16] we observed the formation of spinel in core–shell metal oxide nanofibers. These spinel-type mixed oxides align with the expected interdiffusion and solid-state reactions between the iron and zinc components during the thermal processing of the core–shell nanofibers. The Raman spectra of FeNi33–35 should be analysed in more detail.

In their Raman spectra (Fig. 2b), the Raman peaks at 460–480 $cm^{-1}$ and 560–580 $cm^{-1}$ could be also related to the Ni–O vibrations in the NiO, $NiFe_2O_4$ and $FeNi_2O_4$ crystalline lattices.[45–50] The peak at 675–692 $cm^{-1}$ could be associated with the Fe–O vibrations in the $Fe_3O_4$, $NiFe_2O_4$ and $FeNi_2O_4$ crystalline lattices.[46–48] We observed a significant decrease in the intensity of the Raman peaks at 198–202 and 325–328 $cm^{-1}$ when the concentration of Ni acetate in the shell increased. This finding could be explained by the phase transfer of $Fe_3O_4$ to the spinel form due to iron interaction with a higher concentration of Ni acetate (Fig. 2b). Thus, the Raman spectra confirm the phase transition of $Fe_2O_3$ to $Fe_3O_4$ and possible formation of spinel *via* the transition of $Fe_3O_4$ to $NiFe_2O_4$ and $FeNi_2O_4$ in the core of the fibers.

The TEM images of the shell are shown in Fig. 3. The linear dimensions of the core and shell are summarized in Table 1.

Fig. 4 presents the TEM-EDS elemental mapping and compositional analysis of the FeNi35 nanowire sample, highlighting distinct differences between the two regions associated with the proposed core–shell structure. The area in Fig. 4a corresponds to the region interpreted as the core, where EDS

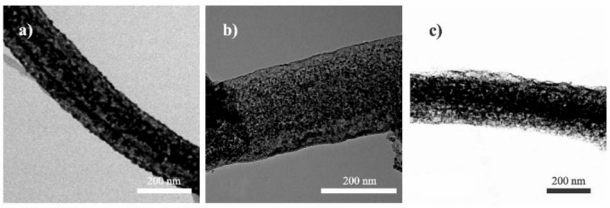


Fig. 3 TEM images of (a) FeNi33, (b) FeNi34 and (c) FeNi35.

Table 1 Dimensions of the core diameter and shell thickness of the core–shell nanofibers

| | Core | Shell |
|---|---|---|
| FeNi31 | 174 ± 15 nm | 13 ± 7 nm |
| FeNi33 | 172 ± 12 nm | 23 ± 12 nm |
| FeNi35 | 178 ± 22 nm | 36 ± 15 nm |

mapping reveals a higher concentration of iron relative to nickel, with the atomic percentage of Fe of 25.20%, Ni of 12.58%, and O of 62.22%. The composite and individual elemental maps show a relatively uniform distribution of oxygen. At the same time, Fe is more abundant than Ni, consistent with an Fe : Ni ratio of approximately 2 : 1. This stoichiometry closely matches that of $Fe_2NiO_4$, supporting the identification of this region as the outer shell of the nanowire. In contrast, the area in Fig. 4b corresponds to the nanowire shell, where the EDS data indicate a reversed elemental ratio with Fe of 15.08%, Ni of 29.07%, and O of 55.84%. The Ni-rich composition aligns well with the stoichiometry of $FeNi_2O_4$, suggesting that this region forms the core of the nanowire. In both regions, oxygen is homogeneously distributed, indicating complete oxidation. The EDS spectra further confirm these trends, with the area in Fig. 4a showing a dominant Fe signal and the area in Fig. 4b showing a dominant Ni signal, correlating well with the corresponding atomic concentrations. Thus, the mapping, quantitative data, and spectral profiles provide compelling evidence of a compositional gradient consistent with an FeNi-based core–shell nanostructure.

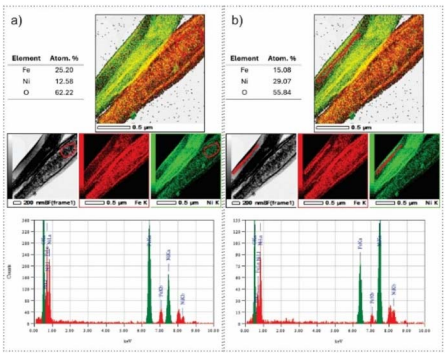


Fig. 4 TEM-EDS elemental maps of Fe, Ni and O taken from the area of (a) core and (b) shell of the FeNi 35 sample (EDS analysis was performed for the area selected by red circles).

The XPS results are presented in Fig. 5a–c. Deconvolution of the Fe $2p_{1/2}$ and Fe $2p_{3/2}$ peaks showed the presence of the $Fe^{3+}$ and $Fe^{2+}$ oxidation states with binding energies of 725 eV ($Fe^{3+}$)/723 eV ($Fe^{2+}$) and 711 eV ($Fe^{3+}$)/709 eV ($Fe^{2+}$), respectively.[51] Deconvolution of the Ni $2p_{1/2}$ and Ni $2p_{3/2}$ peaks showed the presence of the $Ni^{3+}$ and $Ni^{2+}$ oxidation states with binding energies of 872.9 eV ($Ni^{3+}$)/871.6 eV ($Ni^{2+}$) and 855.7 eV ($Ni^{3+}$)/854.2 eV ($Ni^{2+}$), respectively.[52,53] Deconvolution of the O 1s peaks showed characteristic peaks at 529.5 eV and 531 eV,

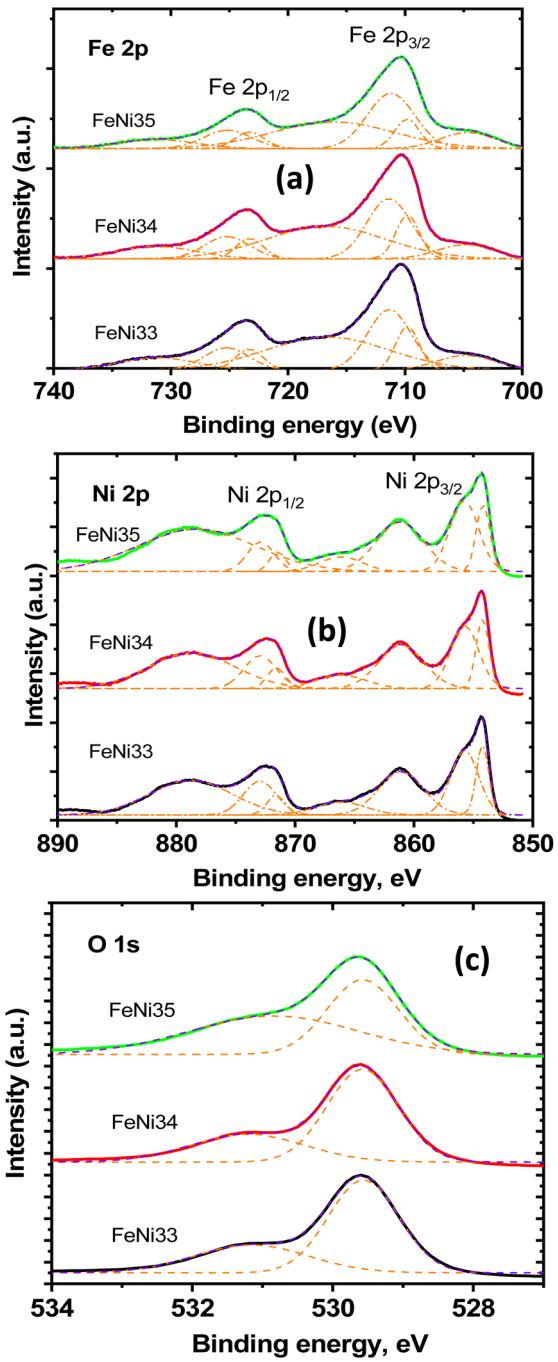


Fig. 5 Structural properties of the core–shell nanofibers measured by XPS: (a) Fe 2p: 1-FeNi33, 2-FeNi34, and 3-FeNi35; (b) Ni 2p: 1-FeNi33, 2-FeNi34, and 3-FeNi35; and (c) O 1s: 1-FeNi33, 2-FeNi34, and 3-FeNi35.

Table 2 Summary of the XPS peak area ratios

| Sample | $Ni^{3+}$ $2p_{3/2}$/$Ni^{2+}$ $2p_{3/2}$ | $Fe^{3+}$ $2p_{3/2}$/$Fe^{2+}$ $2p_{3/2}$ | (O 1s 529 eV)/(O 1s 530 eV) |
|---|---|---|---|
| FeNi33 | 2.07 | 2.58 | 2.074 |
| FeNi34 | 1.96 | 2.57 | 2.082 |
| FeNi35 | 2.23 | 3.62 | 1.82 |
| $Fe_2O_3$ | — | 1.53 | 1.69 |
| NiO | 2.47 | — | 2.28 |

corresponding to lattice oxygen and defect states/adsorbed surface oxygen/water, respectively.[52]

The presence of two oxidation states, $Ni^{3+}/Ni^{2+}$ and $Fe^{3+}/Fe^{2+}$, explains the phase transitions and formation of defects in the core–shell metal oxide nanofibers.[52,54] Particularly, in the case of NiO, the XPS ratio of $[Ni^{3+}/Ni^{2+}]$ is denoted as a key parameter for the formation of a spinel phase and defects in the NiO structure.[54] To evaluate the presence of defects in the core–shell nanofibers, the calculated ratios of the XPS peaks for $Ni^{3+}/Ni^{2+}$, $Fe^{3+}/Fe^{2+}$ and oxygen are summarized in Table 2.

Based on the obtained results, the concentration of defects and part of the spinel phase in the NiO layer increased with an increase in the concentration of Ni acetate and achieved the highest value for the FeNi35 sample.[54,55]

The $Fe^{3+}/Fe^{2+}$ ratio increased from sample Fe33 to Fe35. This finding matches the higher possibility of the formation of $NiFe_2O_4$ rather than of $FeNi_2O_4$ when the concentration of Ni acetate increased.

The (O 1s: 529 eV)/(O 1s: 531 eV) ratio shows part of the stoichiometric metal oxide. This ratio is a parameter defining the forming of defects. The reduced ratios (O 1s 529 eV)/(O 1s 531 eV) for the NiO shell confirm our assumption about the intense formation of defects in NiO[54,55]

The XPS analysis of the $Fe_2O_3$ nanofibers and NiO nanotubes is shown in Fig. 1Sa–d. Deconvolution of the peaks of Fe $2p_{1/2}$ and Fe $2p_{3/2}$ showed the presence of the $Fe^{3+}$ and $Fe^{2+}$ oxidation states with binding energies of 725 eV ($Fe^{3+}$)/723 eV ($Fe^{2+}$) and 711 eV ($Fe^{3+}$)/710 eV ($Fe^{2+}$), respectively. Deconvolution of the Ni $2p_{1/2}$ and Ni $2p_{3/2}$ peaks showed the presence of the $Ni^{3+}$ and $Ni^{2+}$ oxidation states with binding energies of 872.95 eV ($Ni^{3+}$)/871.1 eV ($Ni^{2+}$) and 855.6 eV ($Ni^{3+}$)/853.7 eV ($Ni^{2+}$), respectively. Deconvolution of the O 1s peaks showed characteristic peaks at 529.8 eV, 531, 531.7 and 533 eV for $Fe_2O_3$ and 529.8 eV, 531.2, 532.5 and 533.7 eV for $Fe_2O_3$ and 531 eV, corresponding to lattice oxygen and defect states/adsorbed surface oxygen/water, respectively. The ratios of the $Ni^{3+}/Ni^{2+}$, $Fe^{3+}/Fe^{2+}$ and oxygen peaks are summarized in Table 2. Due to the different chemical compositions of $Fe_2O_3$ and $Fe_3O_4$, it is hard to compare the $Fe^{3+}/Fe^{2+}$ oxygen peak ratios. The Ni ratio of $Ni^{3+}/Ni^{2+}$ in pure NiO was sufficiently higher in a single nanofiber, indicating a higher concentration of Ni-based defects. However, the ratio of the deconvoluted XPS peaks of oxygen for pure NiO showed a higher value compared to that of FeNi33–35, consistent with the less defect structures of oxygen vacancies in the single nanofibers. XPS of the single $Fe_2O_3$ nanofibers and NiO nanotubes did not show evidence of the formation of $NiFe_2O_4$ in the interface between the core and shell.

Closer inspection, supported by the TEM-EDS data (Fig. 4), revealed additional contributions from iron nickel oxide phases, specifically $FeNi_2O_4$ (ICSD 01-074-6507) and $Fe_2NiO_4$ (ICSD 01-071-3850). These mixed-oxide phases have similar crystallographic parameters and space groups (*e.g.*, $Fd\bar{3}m$ for $FeNi_2O_4$), leading to overlapping diffraction peaks with that of $Fe_3O_4$ and NiO, complicating their straightforward identification in the XRD patterns.

The optical properties of the core–shell metal oxide nanofibers were investigated *via* diffuse reflectance spectroscopy (Fig. 6a). The core–shell nanofibers had a wide absorption range from 550 to 740 nm with two characteristic slopes. The measured diffuse reflectance, $R$, was recalculated to the Kubelka–Munk coefficient, $F$, as follows:[56]

$$F = \frac{(1-R)^2}{2 \times R} \quad (3)$$

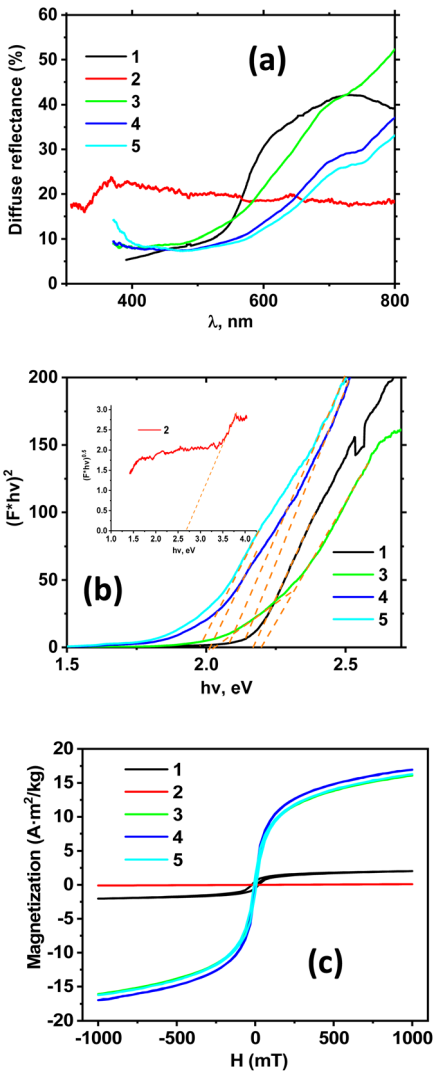


Fig. 6 Characterization of the optical and magnetic properties of the core–shell nanofibers: (a) diffuse reflectance spectra: 1-FeNF, 2-NiNT, 3-FeNi33, FeNi34, and FeNi35; (b) calculation of band gap: 1-FeNF, 2-NiNT, 3-FeNi33, FeNi34, and FeNi35; and (c) magnetic properties: 1-FeNF, 2-NiNT, 3-FeNi33, 4-FeNi34, and 5-FeNi35.

The band gap, $E_g$, of the control sample $Fe_3O_4$ and the core–shell nanofibers was calculated using the Tauc plot for the direct optical transitions, as follows:[57]

$$(F \times hv)^2 = A \times (hv - E_g) \quad (4)$$

where $A$ and $hv$ are a constant and photon energy, respectively (Fig. 6b). In the NiO control samples, the power coefficient in eqn (4) changes to 0.5. It should be emphasized that the Tauc plot with a power coefficient of 0.5 was only applicable for NiO (Fig. 6b, curve 2). The iron oxide nanofibers and core–shell nanofibers showed direct optical transitions.

The band gap values were calculated using the linear slopes in Fig. 1S, as follows: 2.18 eV ($Fe_2O_3$), 2.76 eV (NiO), 2.1 eV and 2.23 eV (FeNi33), 2.01 eV and 2.15 eV (FeNi34), and 1.9 eV and 2.13 eV (FeNi35).

It is known that $Fe_2O_3$ nanostructures have a direct band bap in the range of 2–2.5 eV.[58,59] The band gap energy of $Fe_3O_4$ is in the range of 2–2.2 eV.[60] NiO has a high band gap energy (2.8–4.5 eV) depending on its preparation, crystallinity and defect concentration.[55,58,61,62]

It was shown that defects in NiO reduced its band gap.[55,63,64] The core–shell nanofibers showed two band gaps with average values of 2.02 eV and 2.2 eV, corresponding to $Fe_2NiO_4$ and $Fe_3O_4$, respectively.[65,66] Due to presence of $Fe_2NiO_4$ and $Fe_3O_4$ with band gaps lower than 2.4 eV, the fabricated core–shell nanofibers absorb more light compared to bare $Fe_2O_3$. The absorption by the nanofibers depends on the $Fe_2NiO_4/Fe_3O_4$ ratio. This could be varied by changing the concentrations of Fe and Ni precursors in the core and shell and increasing the annealing temperature, promoting the formation of $Fe_2NiO_4$. Based on this, the absorption spectra of the core–shell nanofibers could cover a higher spectral interval in the visible range, which opens perspectives for their photocatalytic application.

The FeNi33, FeNi34 and FeNi35 samples all display a considerable response to a magnetic field. The magnetization curves of the samples, as well as the $Fe_2O_3$ nanofibers and NiO nanotubes are given in Fig. 6b. The magnetic properties of the samples are dominated by their iron oxide content, as demonstrated by a comparison of the curves of the NiO nanotubes and pure iron oxide nanofibers. The samples are ferromagnetic, with pronounced hysteresis.

The Raman, XPS, and TEM characterization showed that the core of the nanofibers consists of $FeNi_2O_4$ and $Fe_3O_4$. The spinel ratio increased with an increase in the Ni acetate concentration as more $Fe_3O_4$ could transform into spinel.

The photocatalytic activity of FeNi33, FeNi34, and FeNi35 was systematically evaluated through the degradation of two model pollutants, methylene blue (MB) and acetaminophen (ACT), each at an initial concentration of 10 mg $L^{-1}$ in aqueous solution (pH = 7).

The photodegradation experiments were conducted under visible light exposure for durations of 3.5 h for MB and 6 h for ACT.

MB and ACT were selected as representative contaminants due to their extensive global use and frequent detection in natural and wastewater environments. Both compounds exhibit

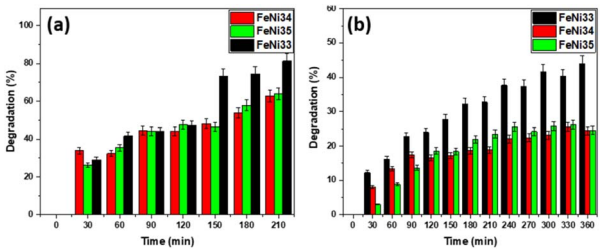


Fig. 7 Visible-light degradation of methylene blue (a) and acetaminophen (b) using FeNi33, FeNi34, and FeNi35 catalysts.

substantial resistance to photodegradation in the absence of a catalyst, making them suitable indicators for assessing the photocatalytic performance.[5,36]

Following 3.5 h of visible light irradiation, the degradation efficiencies of MB were 81.35% for FeNi33, 63.90% for FeNi35, and 62.89% for FeNi34 (Fig. 7a). In the case of ACT, the degradation observed after 6 h was 44.08% for FeNi33, 24.42% for FeNi34, and 24.57% for FeNi35 (Fig. 7b). These results clearly demonstrate the comparatively enhanced photocatalytic efficiency of FeNi33, particularly in the degradation of both pollutants under visible light.

In contrast, increasing the nickel acetate content in FeNi34 and FeNi35 resulted in a measurable decline in photocatalytic efficiency. This trend highlights the influence of the NiO shell thickness and composition on the charge transport and interfacial behavior. The XPS results revealed a higher $Ni^{3+}/Ni^{2+}$ ratio with increased nickel content, indicating a higher layer of spinel.[67,68] Although a moderate level of spinel can enhance the visible light absorption and promote charge separation through the introduction of a p–n junction with $Fe_3O_4$, an excessive thickness of spinel prevents charge transfer to the NiO surface layer, thereby hindering the photocatalytic activity.[67] A thicker spinel interface layer may also obstruct efficient electron transfer across the $Fe_3O_4/NiFe_2O_4/NiO$ interface, potentially introducing interfacial energy barriers that impair the charge mobility. This is especially relevant in core–shell structures, where their optimal photocatalytic performance depends on a delicate balance among shell coverage, structural integrity, and defect engineering.[69] FeNi33 appears to offer this balance, with its intermediate $NiFe_2O_4$ content providing sufficient n–p–p junction formation and defect-mediated enhancement without crossing into the regime of detrimental recombination. These observations underscore the critical role of core–shell design in tailoring the optical and electronic properties of core–shell nanomaterials for effective photocatalytic applications.

The kinetics for the degradation of methylene blue (MB) under visible light irradiation were evaluated using a pseudo-first-order kinetic model, as supported by the high linearity of the fitted curves and correlation coefficients ($R^2$ values) approaching unity (Fig. 10a and b). Among the investigated materials, FeNi33 exhibited the highest photocatalytic activity, as reflected by its rate constant of 0.0018 $min^{-1}$ compared to that of 0.0011 $min^{-1}$ and 0.0010 $min^{-1}$ for FeNi34 and FeNi35, respectively. This enhanced performance can be attributed to

the synergistic interaction between NiO and $Fe_2NiO_4$–$Fe_3O_4$ within the core–shell architecture of FeNi33, which facilitates improved charge separation and interfacial charge transport. Consistent photocatalytic behaviour was also observed in the degradation of acetaminophen (ACT), where FeNi33 again demonstrated a superior kinetic performance with a rate constant of 0.0077 $min^{-1}$, surpassing that of FeNi35 (0.0050 $min^{-1}$) and FeNi34 (0.0048 $min^{-1}$). These results highlight the importance of compositional and structural optimization in achieving efficient photocatalytic activity under visible light conditions.

It is worth noting that due to the phase transitions between the core–shell nanofibers FeNF of $Fe_2O_3$ → $Fe_3O_4$, fibers with different chemical compositions and catalytic properties were fabricated. This is the novelty of our fabrication method, restricting the fabrication of control nanofiber samples. According to the literature, $Fe_3O_4$ showed good a photocatalytic performance for the degradation of dyes and APC when combined with other materials to improve the separation of photogenerated charges.[70,71] The photocatalytic applications of NiO nanostructures show that they are efficient only under UV light excitation or in combination with other nanomaterials.[72–74] A zone diagram of the developed core–shell nanofibers is presented in Fig. 8. This diagram is based on the electron affinity of $Fe_3O_4$ (5.3 eV)[75,76] and NiO (2.5).[77] The electron affinity of $NiFe_2O_4$ is not presented in the literature. We used the values of the work function (5.1 eV) and valence band position ($E_f - E_v =$ 0.75 eV) reported in.[78] According to the diagram, the n–p–p structure will be formed, possessing the layer thicknesses of $d_1$, $d_2$, $d_3$, corresponding to $Fe_3O_4$, $NiFe_2O_4$ and NiO, respectively.

Mott–Schottky spectroscopy is a powerful method to analyse the charge transfer in complex compounds, such as core–shell nanostructures.[79] Investigation of the conductivity type and flat band potential of the single $Fe_2O_3$ and NiO nanofibers is shown in Fig. 9a and b, respectively. It was found that the $Fe_2O_3$ nanofibers and NiO nanotubes showed n- and p-type conductivity, respectively.[80,81] The flat band potentials of the $Fe_2O_3$ nanofibers and NiO nanotubes were calculated according to the following equation:[16]

$$\frac{1}{C^2} = \frac{2}{\varepsilon\varepsilon_0 N_d A^2}\left(E - E_{fb} - \frac{k_B T}{q}\right) \quad (5)$$

where $C$ is the capacitance of the space charge layer, $\varepsilon$ is the dielectric constant of the ZnO layer, $\varepsilon_0$ is the vacuum permittivity, $q$ is the elementary charge, $N_d$ is the donor density, $A$ is the square of the electrode immersed in the electrolyte, $E$ is the applied potential, $E_{fb}$ is the flat-band potential, $k_B$ is the Boltzmann constant, and $T$ is the temperature.

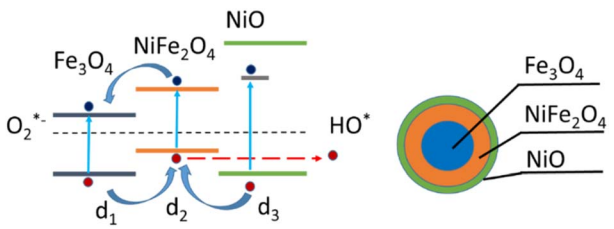


Fig. 8 Zone diagram of developed core–shell nanofibers.

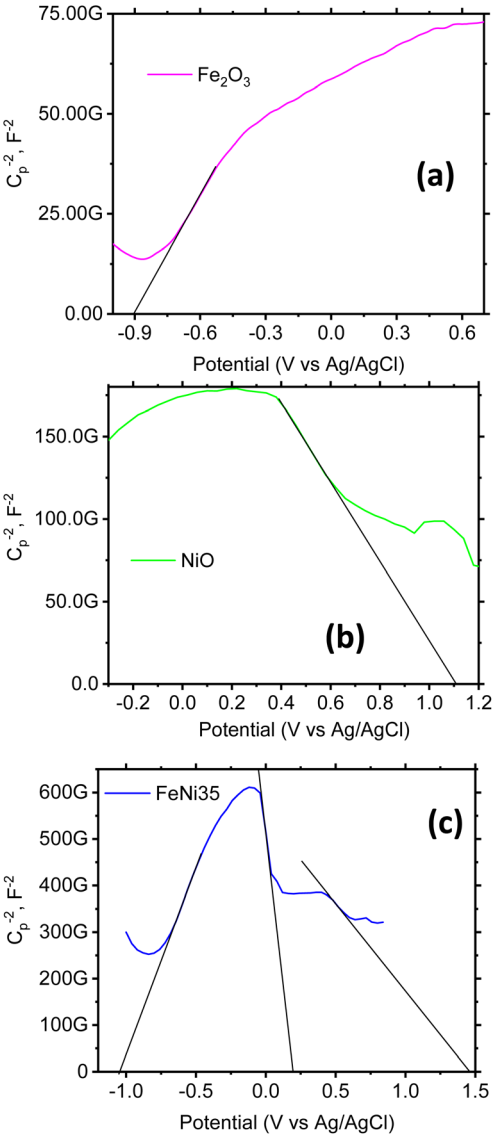


Fig. 9 Mott–Schottky spectra: (a) $Fe_2O_3$ nanofibers, (b) NiO nanotubes, and (c) FeNi35.

The calculated flat band potentials are shown in Table 3.

FeNi investigated by Mott–Schottky spectroscopy showed different behaviors from singe iron and nickel oxide nanofibers.[82,83] In FeNi35, we identified three characteristic parts related to $Fe_3O_4$,[84] $Fe_2NiO_4$ (ref. 85) and NiO.[81] The calculated flat band potentials are shown in Table 3. Based on the comparison of the single nanofibers, the flat band potentials increased due to the formation of a p–n junction.[82,83]

The comparison of the $1/C^2$ values of the $Fe_2O_3$, NiO and FeNi35 samples show a significant increase in the $1/C^2$ value due to the formation of a depleted layer after forming the $Fe_3O_4$/$NiFe_2O_4$/NiO n–p–p junction.[79] The Mott–Schottky measurements confirm the proposed scheme of the photogenerated charge transfer between the core/shell interface.

Table 3 Calculated flat band potential values

| | Built in potential, *V* |
|---|---|
| $Fe_2O_3$ | −1.15 |
| NiO | +1.12 |
| FeNi35 | −1.3, 0.35, 1.2 |

Light-induced transitions form electrons and holes in $Fe_3O_4$ and $NiFe_2O_4$. In NiO, holes are formed due to the transition between its valence band and defect states. Significant charge separation is formed in between $Fe_3O_4$ and $NiFe_2O_4$, directing holes to the $NiFe_2O_4$ layer. Based on the zone diagram, the photogenerated holes will migrate to the surface through the $NiFe_2O_4$/NiO interface and participate in photocatalytic reactions. The photocatalytic properties are defined by the relation of $d_1/d_2/d_3$. When the concentration of Ni acetate increases, more phase transitions are recorded following the order of $d_2 > d_1 > d_3$. In this situation, holes are located in the bulk of the fiber and its photocatalytic activity is low. When the concentration of Ni acetate decreases in the order of $d_1 > d_2 > d_3$, the photocatalytic activity increases due to hole transport to the surface through the $NiFe_2O_4$/NiO interface. Thus, the FeNi33 core–shell nanofibers showed the highest photocatalytic properties for the degradation of MB and APC.

The photocatalytic stability of the FeNi33 nanocomposite was evaluated through five successive degradation cycles of acetaminophen (ACT) and methylene blue (MB), each conducted with an initial pollutant concentration of 10 mg $L^{-1}$ at neutral pH (pH = 7). After each cycle, the catalyst was recovered *via* filtration, thoroughly rinsed with deionized water, and dried at 100 °C, following the procedures reported in previous studies.[5,36] The degradation efficiency of ACT exhibited a modest decline, decreasing from 44.08% in the first cycle to 41.87%, 39.78%, 40.62%, and 42.76% in the subsequent cycles, respectively (Fig. 10c). Similarly, the photocatalytic performance for MB showed a gradual decrease from 81.35% in the first cycle to 78.90%, 77.32%, 76.54%, and 74.24% over the following cycles, respectively. This corresponds to an overall reduction in efficiency of approximately 8% for MB and 3% for ACT across five cycles.

Despite the minor decline in activity, the FeNi33 composite retained a substantial portion of its initial photocatalytic efficiency, thereby demonstrating good reusability and potential for long-term application in visible-light-driven pollutant degradation systems.

Subsequent photocatalytic experiments on ACT degradation were conducted under identical conditions using the optimized FeNi33 composite and in the presence of specific scavengers, each introduced at a concentration of 0.06 M (ref. 5 and 36) (Fig. 10d). The selected scavengers isopropanol (IPA), benzoquinone (BQ), and ethylenediaminetetraacetic acid (EDTA) were employed to selectively quench hydroxyl radicals ($^{\bullet}OH$), superoxide radicals ($O_2^{\bullet-}$), and photogenerated holes ($h^+$), respectively. The degradation efficiency of ACT was markedly reduced upon the addition of these quenchers, with observed inhibition rates of 29.6% (IPA), 37.1% (BQ), and 27.3%

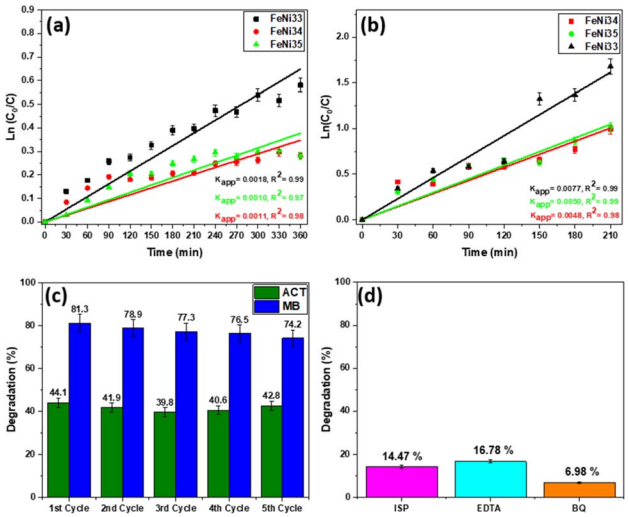


Fig. 10 Degradation, repeatability and photocatalysis scavenging tests of the core–shell nanofibers: (a) kinetics of acetaminophen degradation in the presence of FeNi33, FeNi34, and FeNi35, (b) kinetics of methylene blue degradation in the presence of FeNi33, FeNi34, and FeNi35, (c) recyclability of FeNi33 over five cycles degradation for acetaminophen and methylene blue and (d) photocatalytic degradation of acetaminophen using FeNi33 in the presence of scavengers (EDTA, IPA, and BQ).

(EDTA). These results clearly suggest that reactive oxygen species (ROS), particularly superoxide radicals and photogenerated holes, play dominant roles in the photocatalytic oxidation of ACT under visible light, while hydroxyl radicals also contribute to a lesser extent.

According to the literature, $Fe_2O_3$ is not a good material for the degradation of MB and paracetamol.[86–88]

The performance reported by the presented papers showed a long degradation time or insufficient degradation due to dye photolysis. In our case, $Fe_2O_3$ did not show a good performance in the photodegradation of MB and paracetamol (less than 5%). Due to their high band gap, NiO nanotubes do not have good perspectives for visible light applications. To validate this, the photocatalytic performance of $Fe_2O_3$ and NiO in the degradation of paracetamol was studied, as presented in Fig. 2S. According to the control measurements, we can conclude that the core–shell nanofibers show good perspectives for application in visible light photocatalysis.

# 4 Conclusion

The novel core–shell metal oxide nanofibers developed *via* coaxial electrospinning exhibit promising optical, magnetic and photocatalytic properties. The p–n core–shell heterojunction of iron oxide and nickel oxide showed higher light absorption in the visible range and higher magnetisation compared to single-mode iron and nickel oxide nanofibers. The photocatalytic properties of the novel core–shell metal oxide nanofibers depend on the structure and interface between their core and shell. Due to the phase transition of $Fe_3O_4 \rightarrow Fe_2NiO_4$, the $Fe_3O_4$–$Fe_2NiO_4$/NiO architecture was formed in the developed

core–shell nanofibers. Efficient separation of photogenerated charges between the core and shell was a key factor in the photocatalytic degradation of methylene blue and acetaminophen. The spinel interlayer can capture the photogenerated charge and block the charge transfer to the surface of the shell. Therefore, the highest photocatalytic performance was observed for the fibers with the lowest Ni acetate concentration and a lower spinel fraction. The advanced properties of the novel $Fe_3O_4$–$Fe_2NiO_4$/NiO core–shell nanofibers enable their future applications in the photocatalytic purification of industrial water from APC by using visible light. However, the developed fibers did not show the highest degradation rate towards methylene blue and acetaminophen reported to date. The photocatalytic activity of the $Fe_3O_4$–$Fe_2NiO_4$/NiO core–shell nanofibers could be improved by optimization of the thickness of their spinel layer. Co-axial electrospinning, as a facile and low cost method, enables the properties of core and shell solutions to be varied. This paper opens new prospects to the development of new functional nanomaterials *via* a low cost and efficient fabrication method.

## Author contributions

Conceptualization – R. V., M. A., M. B.; data curation – T. M. H, V. Z., I. T., V. S., A. D.; formal analysis – R. V., M. A., T. M. H., V. S., D. E., A. F., S. R., R. H., D. C., M. B.; funding acquisition – R. V., M. S., D. E., A. F., S. R., R. H., D. C., M. B; investigation – R. V., M. A., T. M. H., V. Z., M. S., M. C., I. T., V. S., A. D.; methodology – R. V., M. A., T. M. H., V. Z., M. S., M. C., I. T., V. S., A. D., M. B.; project administration – R. V., M. S., D. E., A. F., S. R., R. H., D. C., M. B.; resources – R. V., M. A., M. S., D. E., A. F., S. R., R. H., D. C., M. B.; supervision – R. V., M. A., D. E., A. F., S. R., R. H., D. C., M. B.; validation – R. V., M. A., T. M. H., A. F., S. R., R. H., D. C., M. B., visualization – R. V., M. A., T. M. H., V. Z., M. S., M. C., I. T., V. S., A. D., D. E., A. F., writing – original draft – R. V., M. A, T. M. H., V. Z., M. S., M. C., I. T., V. S., A. D., D. E., A. F., S. R., R. H., D. C., M. B.; writing – review & editing – R. V., M. A., T. M. H., V. Z., A. F., S. R., R. H., D. C., M. B.

## Conflicts of interest

There are no conflicts to declare.

## Data availability

XRD, Raman, diffuse reflectance and XPS data are reposited as Excel file in Zenodo **https://doi.org/10.5281/zenodo.15708152**.

Supplementary information (SI) is available. See DOI: **https://doi.org/10.1039/d5ra04859a**.

## Acknowledgements

R. V. acknowledges the fundamental and applied research projects of the Latvian Council of Science 'Novel core–shell nanofibers formed by co-axial electrospinning for photocatalytic applications' (lzp-2021/1-0140). A. F. and M. S. acknowledge HE-MCSA-RISE-2021, Sens4Corn, grant number 101086364.

## References

1 A. A. Nada, B. O. Orimolade, H. H. El-Maghrabi, B. A. Koiki, M. Rivallin, M. F. Bekheet, R. Viter, D. Damberga, G. Lesage, I. Iatsunskyi, E. Coy, M. Cretin, O. A. Arotiba and M. Bechelany, *Appl. Mater. Today*, 2021, **24**, 101129.
2 E. Makhoul, F. Tanos, M. F. Bekheet, W. Riedel, E. Petit, R. Viter, I. Tepliakova, A. Ramanavicius, A. Razzouk, G. Lesage, M. Cretin, M. Boulos, D. Cornu and M. Bechelany, *Environ. Sci.: Nano*, 2023, **10**, 3156–3170.
3 S. Sayegh, M. Abid, F. Tanos, M. Cretin, G. Lesage, F. Zaviska, E. Petit, B. Navarra, I. Iatsunskyi, E. Coy, R. Viter, V. Fedorenko, A. Ramanavicius, A. Razzouk, J. Stephan and M. Bechelany, *Colloids Surf., A*, 2022, **655**, 130213.
4 F. Tanos, E. Makhoul, A. A. Nada, M. F. Bekheet, W. Riedel, S. Kawrani, H. Belaid, E. Petit, R. Viter, V. Fedorenko, A. Ramanavicius, M. Boulos, D. Cornu, A. Razzouk, G. Lesage, M. Cretin and M. Bechelany, *Appl. Surf. Sci.*, 2024, **656**, 159698.
5 M. Abid, T. M. Howayek, O. Mazur, R. Viter, M. F. Bekheet, A. A. Nada, D. Bezzerga, J. Hong, P. Miele, I. Iatsunskyi, E. Coy, G. Lesage, R. Habchi, D. Cornu and M. Bechelany, *Colloids Surf., A*, 2025, **709**, 136077.
6 H. Rafieipour, M. R. Vaezi and A. Kazemzadeh, *Micro Nano Lett.*, 2016, **11**, 707–711.
7 S. Sayegh, F. Tanos, A. Nada, G. Lesage, F. Zaviska, E. Petit, V. Rouessac, I. Iatsunskyi, E. Coy, R. Viter, D. Damberga, M. Weber, A. Razzouk, J. Stephan, M. Bechelany, S. Sayegh, F. Tanos, A. Nada, G. Lesage, F. Zaviska, E. Petit, V. Rouessac, I. Iatsunskyi and E. Coy, *Dalton Trans.*, 2022, **51**, 2674–2695.
8 E. Mahmoudi and M. A. Behnajady, *Colloids Surf., A*, 2018, **538**, 287–296.
9 K. G. Nair, R. Vishnuraj and B. Pullithadathil, *Adv. Mater.*, 2022, **3**, 443–455.
10 T. Sukumar and K. Kadirvelu, *ChemistrySelect*, 2022, **7**, e202201679.
11 X. Zhang, V. Aravindan, P. S. Kumar, H. Liu, J. Sundaramurthy, S. Ramakrishna and S. Madhavi, *Nanoscale*, 2013, **5**, 5973–5980.
12 S. K. Sahoo, G. K. Panigrahi, J. P. Dhal, J. K. Sahoo, A. K. Behera, P. C. Panda, P. Patel, S. K. Mund, S. M. Muduli and L. Panda, *Colloids Surf., A*, 2022, **652**, 129877.
13 L. Fu, J. Xu, Q. Liu, C. Liu, S. Fan, S. Ramakrishna and W. Tang, *Ceram. Int.*, 2024, **50**, 3443–3452.
14 A. Gangan, A. Fahmy, S. A. Shaban and Z. M. El-Bahy, *Adv. Compos. Hybrid Mater.*, 2025, **8**, 1–20.
15 Q. Chen, J. Liu, L. Tang, Z. Zeng and B. Zhu, *J. Environ. Chem. Eng.*, 2024, **12**, 112422.
16 A. Lys, V. Zabolotnii, M. Čaplovičová, I. Tepliakova, A. Berzins, M. Sahul, Ľ. Čaplovič, A. Pogrebnjak, I. Iatsunskyi and R. Viter, *J. Alloys Compd.*, 2024, **984**, 173885.

17 E. C. Okpara, O. C. Olatunde, O. B. Wojuola and D. C. Onwudiwe, *Environ. Adv.*, 2023, **11**, 100341.
18 A. Krishnan, A. Swarnalal, D. Das, M. Krishnan, V. S. Saji and S. M. A. Shibli, *J. Environ. Sci.*, 2024, **139**, 389–417.
19 W. Wang, Y. H. Zhou, P. K. Sun, L. G. Liu, C. Bin Guo, X. L. Wang, T. F. Zhang, Y. N. Cong and Z. B. Wei, *Vacuum*, 2024, **228**, 113526.
20 P. P. Sethy, T. K. Pani, S. Rout and B. Sundaray, *J. Mater. Sci.: Mater. Electron.*, 2023, **34**, 1–15.
21 P. P. Sethy and B. Sundaray, *Nanotechnology*, 2023, **34**, 445701.
22 L. Li, Y. Bao, S. Jiang, X. Yan, H. Shao, Q. Ma, W. Yu, J. Wang, X. Dong and B. Yue, *Adv. Funct. Mater.*, 2025, 2502945.
23 Y. Bao, B. Yue, L. Li, S. Jiang, H. Shao, Y. Xie, Q. Ma, W. Yu, J. Wang and X. Dong, *Chem. Eng. J.*, 2025, **519**, 164965.
24 X. Huo, Y. Xie, Y. Sheng, Y. Hu, H. Qi, H. Shao, Q. Ma, W. Yu, G. Liu and X. Dong, *Matter*, 2025, **8**(3), 101946.
25 F. Sun, Q. Xu, X. Wang, C. Luo, M. Zhao, Q. Ma, H. Yu, W. Yu and X. Dong, *Adv. Funct. Mater.*, 2025, e05795.
26 F. Sun, D. Xu, J. Xu, Y. Xie, H. Qi, F. Liu, H. Shao, H. Yu, W. Yu and X. Dong, *J. Mater. Sci. Technol.*, 2025, **208**, 278–291.
27 F. Sun, H. Qi, Y. Xie, Q. Ma, W. He, D. Xu, G. Wang, W. Yu, T. Wang and X. Dong, *J. Alloys Compd.*, 2020, **830**, 154673.
28 F. Sun, D. Xu, Y. Xie, F. Liu, W. Wang, H. Shao, Q. Ma, H. Yu, W. Yu and X. Dong, *J. Colloid Interface Sci.*, 2022, **628**, 614–626.
29 Q. Xu, F. Sun, X. Liu, Y. Hu, C. Luo, X. Wang, H. Shao, H. Yu, W. Yu and X. Dong, *J. Alloys Compd.*, 2025, **1020**, 179363.
30 F. Sun, Q. Xu, H. Liu, D. Xu, X. Wang, C. Luo, T. Wang, H. Yu, W. Yu and X. Dong, *J. Catal.*, 2024, **440**, 115813.
31 D. Qin, W. Hu and L. Zhang, *Desalin. Water Treat.*, 2024, **317**, 100136.
32 R. Nodehi, H. Shayesteh and A. Rahbar-Kelishami, *Int. J. Environ. Sci. Technol.*, 2022, **19**, 2899–2912.
33 M. Amini, S. M. P. Hosseini and N. Chaibakhsh, *Environ. Sci. Pollut. Res.*, 2023, **30**, 98063–98075.
34 T. Li, C. Yang, X. Rao, F. Xiao, J. Wang and X. Su, *Ceram. Int.*, 2015, **41**, 2214–2220.
35 X. Sun, N. Frey Huls, A. Sigdel and S. Sun, *Nano Lett.*, 2012, **12**, 246–251.
36 M. Abid, S. Sayegh, I. Iatsunskyi, E. Coy, G. Lesage, A. Ramanavicius, A. Ben Haj Amara and M. Bechelany, *Colloids Surf., A*, 2022, **651**, 129696.
37 M. Qayoom, K. A. Shah, A. H. Pandit, A. Firdous and G. N. Dar, *J. Electroceram.*, 2020, **45**, 7–14.
38 E. Aytan, B. Debnath, F. Kargar, Y. Barlas, M. M. Lacerda, J. X. Li, R. K. Lake, J. Shi and A. A. Balandin, *Appl. Phys. Lett.*, 2017, **111**, 252402.
39 R. Jaiswal and K. V. S. Ranganath, *J. Inorg. Organomet. Polym. Mater.*, 2021, **31**, 4504–4511.
40 N. H. Hai, N. D. Phu, N. H. Luong, N. Chau, H. D. Chinh, L. H. Hoang and D. L. Leslie-Pelecky, *J. Korean Phys. Soc.*, 2008, **52**, 1327–1331.
41 M. Baghaie Yazdi, K. Y. Choi, D. Wulferding, P. Lemmens, L. Alff, M. B. Yazdi, K. Y. Choi, D. Wulferding, P. Lemmens and L. Alff, *New J. Phys.*, 2013, **15**, 103032.
42 H. L. Pham, V. D. Nguyen, V. K. Nguyen, T. H. P. Le, N. B. Ta, D. C. Pham, Q. T. Tran and V. T. Dang, *RSC Adv.*, 2021, **11**, 22317–22326.
43 H. G. Gebretinsae, M. G. Tsegay and Z. Y. Nuru, *Mater. Today: Proc.*, 2021, **36**, 566–570.
44 D. Caso, A. Serrano, M. Jaafar, P. Prieto, A. Kamra, C. González-Ruano and F. G. Aliev, *Condens. Matter*, 2024, **9**, 7.
45 N. Mironova-Ulmane, A. Kuzmin, I. Sildos, L. Puust and J. Grabis, *Latv. J. Phys. Tech. Sci.*, 2019, **56**, 61–72.
46 Z. Alhashem, C. Awada, F. Ahmed and A. H. Farha, *Crystals*, 2021, **11**, 613.
47 C. Sedrati, S. Alleg, H. Boussafel and A. Bendali Hacine, *J. Mater. Sci.: Mater. Electron.*, 2021, **32**, 24548–24559.
48 A. Soam, R. Kumar, D. Thatoi and M. Singh, *J. Inorg. Organomet. Polym. Mater.*, 2020, **30**, 3325–3331.
49 D. Liu, D. Li and D. Yang, *AIP Adv.*, 2017, **7**, 15028.
50 B. Sahu, U. K. Panigrahi, S. Chakravarty, S. Hussain and P. Mallick, *Appl. Phys. A:Mater. Sci. Process.*, 2023, **129**, 1–13.
51 Q. Ai, Z. Yuan, R. Huang, C. Yang, G. Jiang, J. Xiong, Z. Huang and S. Yuan, *J. Mater. Sci.*, 2019, **54**, 4212–4224.
52 M. Imran, H. Coskun, N. A. Khan and J. Ouyang, *Appl. Phys. A:Mater. Sci. Process.*, 2021, **127**, 1–8.
53 W. Huang, S. Ding, Y. Chen, W. Hao, X. Lai, J. Peng, J. Tu, Y. Cao and X. Li, *Sci. Rep.*, 2017, **7**(1), 1–11.
54 Y. Yu, M. Pan, Z. Zhang, Z. An, Y. Wang and X. Hu, *Int. J. Hydrogen Energy*, 2023, **48**, 27679–27685.
55 K. Jouini, A. Raouafi, W. Dridi, M. Daoudi, B. Mustapha, R. Chtourou and F. Hosni,Optik (Stuttg), 2019, **195**, 163109.
56 S. Kawrani, M. Boulos, M. F. Bekheet, R. Viter, A. A. Nada, W. Riedel, S. Roualdes, D. Cornu and M. Bechelany, *Appl. Surf. Sci.*, 2020, **516**, 146051.
57 S. Choudhary, D. Hasina, M. Saini, M. Ranjan and S. Mohapatra, *J. Alloys Compd.*, 2022, **895**(2), 162723.
58 A. J. Haider, R. Al-Anbari, H. M. Sami and M. J. Haider, *Energy Procedia*, 2019, **157**, 1328–1342.
59 V. S. Leão-Neto, A. C. da Silva, L. P. Camargo, M. R. Da Silva Pelissari, P. R. C. da Silva, P. S. Parreira, M. G. Segatelli and L. H. Dall'Antonia, *J. Mater. Sci.: Mater. Electron.*, 2020, **31**, 16882–16897.
60 S. Delice, M. Isik and N. M. Gasanly, *Chem. Phys. Lett.*, 2024, **840**, 141139.
61 M. Hashem, E. Saion, N. M. Al-Hada, H. M. Kamari, A. H. Shaari, Z. A. Talib, S. B. Paiman and M. A. Kamarudeen, *Results Phys.*, 2016, **6**, 1024–1030.
62 N. M. Hosny, *Polyhedron*, 2011, **30**, 470–476.
63 S. Bhanuchandar, G. Vinothkumar, P. Arunkumar, M. Sribalaji, A. K. Keshri and K. S. Babu, *J. Mater. Sci.*, 2023, **58**, 13136–13153.
64 M. Barwant, V. Karande, P. Basnet, D. Kumar, S. Sargazi, M. Mirzaei, M. S. Jabir, D. Sanap and S. Ghotekar, *J. Sol–Gel Sci. Technol.*, 2024, **111**, 409–420.
65 S. K. Tong, P. W. Chi, S. H. Kung and D. H. Wei, *Sci. Rep.*, 2018, **8**(1), 1–11.
66 K. Dileep, B. Loukya, N. Pachauri, A. Gupta and R. Datta, *J. Appl. Phys.*, 2014, **116**, 103505.

67 J. Zhou, J. Liang, Z. Fan, W. Tan, X. Sun, R. Ding, P. Gao and Y. Zhang, *Int. J. Hydrogen Energy*, 2024, **51**, 770–778.
68 B. Bhagat, S. K. Gupta, D. Mandal, A. A. Gor, R. Bandyopadhyay and K. Mukherjee, *Chem.–Asian J.*, 2024, **19**, e202300841.
69 P. Talebi, H. Singh, E. Rani, M. Huttula and W. Cao, *RSC Adv.*, 2021, **11**, 2733–2743.
70 F. Farahmandzadeh, M. Molaei, S. Salehi and E. Molahosseini, *Colloids Surf., A*, 2024, **685**, 133229.
71 P. Kumar, Z. Y. Deng, P. Y. Tsai, C. Y. Chiu, C. W. Lin, P. Chaudhary, Y. C. Huang and K. L. Chen, *Sep. Purif. Technol.*, 2024, **342**, 126988.
72 S. Yasmeen, L. Burratti, L. Duranti, E. Sgreccia and P. Prosposito, *Nanomaterials*, 2024, **14**, 470.
73 D. Singh, K. M. Batoo, S. Hussain, A. Kumar, Q. H. Aziz, F. S. Sheri, H. Tariq and P. Singh, *RSC Adv.*, 2024, **14**, 2429–2438.
74 V. Singh, R. Sapehia and V. Dhiman, *Inorg. Chem. Commun.*, 2024, **162**, 112267.
75 Z. Viskadourakis, M. L. Paramês, O. Conde, M. Zervos and J. Giapintzakis, *Appl. Phys. Lett.*, 2012, **101**, 033505.
76 H. Aireddy, S. Bhaumik and A. K. Das, *Appl. Phys. Lett.*, 2015, **107**, 232406.
77 M. Ruscello, T. Sarkar, A. Levitsky, G. M. Matrone, N. Droseros, S. Schlisske, E. Sachs, P. Reiser, E. Mankel, W. Kowalsky, N. Banerji, N. Stingelin, G. L. Frey and G. Hernandez-Sosa, *Sustainable Energy Fuels*, 2019, **3**, 1418–1426.
78 S. Das, S. Pramanik, R. G. Nair and A. Chowdhury, *Chem.–Asian J.*, 2025, **20**, e202401402.
79 C. Leon, S. Le Gall, M. E. Gueunier-Farret, A. Brézard-Oudot, A. Jaffre, N. Moron, L. Vauche, K. Medjoubi, E. Veinberg Vidal, C. Longeaud and J. P. Kleider, *Prog. Photovoltaics Res. Appl.*, 2020, **28**, 601–608.
80 R. S. Schrebler, L. Ballesteros, A. Burgos, E. C. Muñoz, P. Grez, D. Leinen, F. Martín, J. R. Ramos-Barrado and E. A. Dalchiele, *J. Electrochem. Soc.*, 2011, **158**, D500.
81 D. Koushik, M. Jošt, A. Dučinskas, C. Burgess, V. Zardetto, C. Weijtens, M. A. Verheijen, W. M. M. Kessels, S. Albrecht and M. Creatore, *J. Mater. Chem. C*, 2019, **7**, 12532–12543.
82 P. Li, M. Zhang, X. Li, C. Wang, R. Wang, B. Wang and H. Yan, *J. Mater. Sci.*, 2020, **55**(33), 15930–15944.
83 S. Ravishankar, J. Bisquert and T. Kirchartz, *Chem. Sci.*, 2022, **13**, 4828–4837.
84 A. Braun, K. Sivula, D. K. Bora, J. Zhu, L. Zhang, M. Grätzel, J. Guo and E. C. Constable, *J. Phys. Chem. C*, 2012, **116**, 16870–16875.
85 S. Yılmaz, Ö. K. Kuyumcu, Ş. S. Bayazit, R. M. Z. Ayaz, D. Akyüz and A. Koca, *J. Solid State Electrochem.*, 2021, **26**(1), 245–255.
86 Y. Liu, H. Yu, S. Zhan, Y. Li, Z. Lv, X. Yang and Y. Yu, *J. Sol–Gel Sci. Technol.*, 2011, **58**(3), 716–723.
87 R. N. Araujo, E. P. Nascimento, H. C. T. Firmino, D. A. Macedo, G. A. Neves, M. A. Morales and R. R. Menezes, *J. Alloys Compd.*, 2021, **882**, 160683.
88 X. H. Vu, L. H. Phuoc, N. D. Dien, T. T. H. Pham and L. D. Thanh, *J. Electron. Mater.*, 2019, **48**(5), 2978–2985.